Automatic landslide mapping from satellite imagery with a topography-driven thresholding algorithm

Massimiliano Alvioli[§], Alessandro C. Mondini, Federica Fiorucci, Mauro Cardinali, Ivan Marchesini
Istituto di Ricerca per la Protezione Idrogeologica,
Consiglio Nazionale delle Ricerche
via Madonna Alta, 126 I-06128, Perugia, Italy
[§] massimiliano.alvioli@irpi.cnr.it

Abstract— **We present an improvement of image classification by "thresholding", using topographic information to determine multiple thresholds. We devised a two-steps procedure for automatic classification into landslide or no landslide categories of a change-detection map obtained from satellite imagery. Requirements of the proposed procedure are knowledge of the occurrence of a landslide event, availability of a pre- and post-event pseudo-stereo image pair and a digital elevation model. The novel feature of the approach is represented by the use of slope units as topographic-aware subsets of the scene within which we apply a multiple thresholding method to classify a landslide class membership tuned on the sole landslide spectral response. The method is fully automatic after site-dependent operations, required only once, are performed, and exhibits improved classification performance with limited training requirements. Our automatic procedure is a step forward towards systematic acquisition of landslide events and real-time landslide mapping from satellite imagery.**

I. INTRODUCTION

The most effective source of information describing a landslide event extension and magnitude in a given region is an event landslide inventory map (eLIM). An eLIM is a key input to derive landslide hazard and risk maps, and its preparation require effective monitoring and fast, cost-efficient mapping tools. More in general, despite their importance, landslide inventory maps cover a limited extension of the landslide-prone areas across the global landmass [1,2].

Landslide inventory maps are best prepared by visual interpretation of stereoscopic aerial images [3]. In the last two decades the images captured by high resolution and very high resolution optical satellites [1,4,5], and synthetic aperture radar [4,6], are becoming a viable replacement of aerial photographs, encouraging research efforts in the direction of developing automatic and semi-automatic classification algorithms to distinguish different land covers, including vegetation, urban areas, water bodies and landslides. Use of LiDAR data for automatic landslide mapping is beyond the scope of this work, mainly because it is not suitable for use within the approach described here, and will not be discussed.

Automatic and semi-automatic landslide mapping require image classification methods, including supervised and unsupervised clustering [7,8], and index thresholding [5,9]. Supervised classification calls for a manual training process which can result difficult and time consuming. Reducing the time and the overall effort required to prepare an eLIM, while increasing the level of automation of the mapping procedure, are key issues to obtain a reliable estimate of the extent and magnitude of landslide events on a routinely basis.

In this work, we focus on a classification method which assigns individual pixels to the generic bare soil class, with a spectral fingerprint corresponding to event landslides [10]. We use a Bayesian-based maximum likelihood (ML) approach to assign each pixel either to the "landslide" or "no landslide" land cover classes by thresholding, the simplest existing decision rule. The procedure requires to single out a numerical value (threshold), among all the values in the image, and to assign the pixels values above (or below) the threshold to a particular class [11]. We used thresholding to classify a change detection (CD) function, obtained from a combination of widely used change detection indices tuned on landslide spectral response. In particular, we devised a multi-threshold approach that takes advantage of the topographic information contained in a slope unit (SU) subdivision of the area under investigation [12,13,14,15]. Using a custom classification threshold within each slope unit allows to overcome limitations posed by the different geometric conditions, dictated by the combination of satellite point of view, sun position, slope orientation and

PeerJ Preprints | https://doi.org/10.7287/peerj.preprints.27067v1 | CC BY 4.0 Open Access | rec: 30 Jul 2018, publ: 30 Jul 2018

inclination. Such conditions can be considered homogeneous within typical individual SUs, while they pose limitations when the CD function values are classified using a single threshold. A large number of false negatives and false positives are inherently introduced by a single threshold. On the other hand, misclassifications may be strongly reduced using multiple thresholds.

II. METHOD AND RESULTS

Our method to automatically identify the pixels belonging to the landslide land cover class relies on the concept of a CD function, denoted here and in Ref. [5] as g_{ls} ("ls" stands for "landslides"), obtained with a simplified ML classifier. Figure 1 summarizes the method developed in Ref. [5], illustrating the two basic steps, updated in this work.

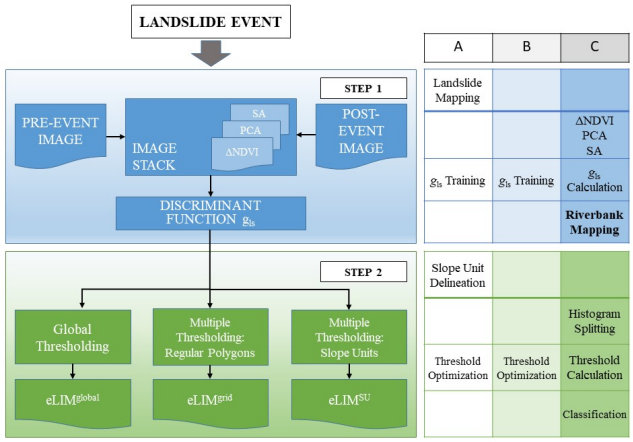

Figure 1. The algorithm proposed in Ref. [5], and updated in this work, applied upon knowledge of the occurrence of a landslide event. Step 1: calculation of the discriminant function; step 2: three different classification possibilities by index thresholding, resulting in three different eLIMs (*cf.* Section II). The table describes the level of automation of the individual operations involved in each of the two steps. A: one-time, site-dependent operations; B: operations that can be optionally performed again in a new study area; C: fully automatic operations, to which we added "Riverbank Mapping" in this work, with respect to Ref. [5].

In the first step, we define the function g_{ls} whose values represent the ML distance of each pixel from the landslide class, providing a pixel-by-pixel measure of the presence or absence of new landslides. The g_{ls} function is obtained measuring changes occurred between a pre- and a post-event image, using three different metrics: changes of NDVI [16], Spectral Angle (SA) [17,18,19] and Principal Component Analysis (PCA) [18]. The three metrics were combined in a single image stack of changes for the analysis.

In the second step, a map is generated by evaluating the g_{ls} function in each pixel of the study area. Then the g_{ls} map pixels are classified as "landslide" or "no landslide", either by: (i) thresholding the g_{ls} values, i.e., selecting as landslides the pixels with g_{ls} values larger than a single threshold value over the whole study area; (ii) using multiple threshold values, within square and rectangular subsets of the g_{ls} map; (iii) as in (ii), but replacing regular subsets with irregular SU polygons, thus introducing local geomorphological information.

In the first step, the innovative feature is represented by the fact that we only aim at defining the landslide class, thus we only need to train the procedure once. In the test case of Ref. [5], the calibration area was selected in only one (big) landslide, for a total of 421 pixels (about 10,000 m^2 out of about 1,000 km^2) in the stack of changes.

In the second step, the core innovation of the procedure is the application of thresholding g_{ls} values within a large number of subsets of the study area, singled out either with and without a topographic information. Existing thresholding approaches use a single threshold, necessarily reducing accuracy, while SU provide local topography information and allows to find local custom thresholds.

The proposed method was tested in an area of about 1,000 m^2 in Myanmar, where torrential rainfall triggered extensive landslides in 2015, including the massive Tonzang landslide and the large number of fatalities [21].

Figure 2 shows histograms of the values for the CD discriminant function g_{ls}. A distinctive feature of the global histogram, Fig. 2(a), is a bi-modal behavior, characterized by a small peak around $g_{ls} = 0$, overwhelmed by a broad peak containing the vast majority of pixels with spectral properties dissimilar from the landslide ones. The two peaks (modes) are separated by a well-defined local minimum, occurring at some g_{ls} value denoted as M. The first approximation to a binary classification of the g_{ls} values is to flag as "landslide" the pixels with $M < g_{ls} < 0$, and to flag as "no-landslide" the remaining pixels.

The next approximation we discuss consists in tracing a grid onto the g_{ls} map, calculate a histogram of the values of g_{ls} for each rectangular polygon singled out by the grid (*cf.* Fig. 2(b)-(e)), and process the histogram with the automatic, non-parametric mode detection software of Ref. [18], implemented as standalone program. Depending on the number and values of the separations between different modes found by the software, we developed an algorithm to determine custom thresholds to be applied within the single polygons we introduced.

PeerJ Preprints | https://doi.org/10.7287/peerj.preprints.27067v1 | CC BY 4.0 Open Access | rec: 30 Jul 2018, publ: 30 Jul 2018

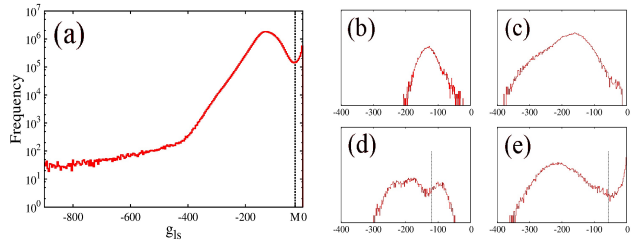

Figure 2. (a): histogram of the g_{ls} function values over the whole study area. (b-d): four sample histograms of the g_{ls} values, corresponding to four individual slope units. The vertical lines represent the divide between different modes, if any. The mode located right from the divide may be due (e), or may not be due (d), to pixels with spectral behavior very similar to pixels known to be within the landslides selected for the training procedure, by construction of g_{ls}.

The third and last approximation is to replace the rectangular polygons with topography-aware slope units. SU were delineated using the automatic software of Ref. [12], using a portion of ASTER digital elevation model, and are shown in Fig. 3 for the calibration study area (about ¼ in size of the whole area). The number and size of SU were chosen maximizing agreement of the automatic classification with an eLIM prepared by expert geomorphologists, by photo-interpretation, in a calibration region. The method was then extended to a different, and wider, validation region. Visual interpretation and g_{ls} analysis were performed on a 5m x 5m RapidEye stereo-pair.

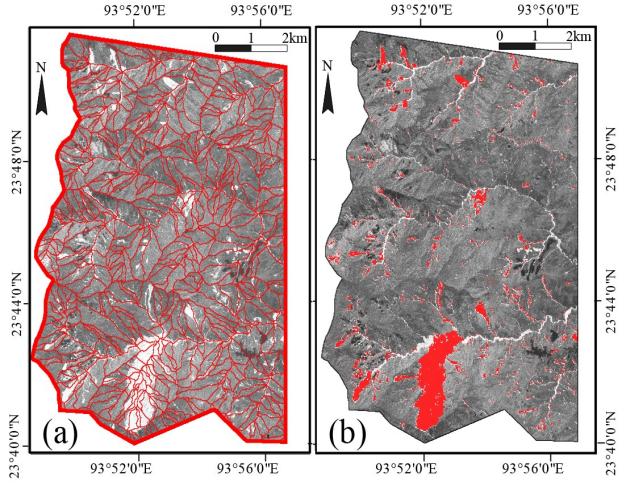

Figure 3. (a): the SU subdivision of the calibration area, in the calibration subset of our test area located in Myanmar (see Ref. [5] for details). (b): red pixels denote the automatically-mapped landslide inventory, eLIM^{SU} (cf. Fig. 1), obtained with multiple thresholds within the SU polygons shown in (a).

In this work, we added an additional level of automation with respect to the work in Ref. [5]. The comparison between automatic and expert mapping was performed everywhere but on pixels corresponding to rivers. We automated riverbanks mapping using a pixel-based method [10,23], thus making the overall method fully automatic after site-dependent operations, required only once, are performed. Such operations are listed in Fig. 1.

We report results of the three different approximations (also reported in Ref. [5]), expressed in terms of an error index E_I, first introduced in Ref. [12] and recently employed as a benchmark for selecting optimal requirements of images from remote sensing for landslide mapping [22]. Results for "grid" and "SU" are obtained with a number of polygons that minimizes E_I in both cases. Results are listed in Table I. The percentage gain of multi-thresholding with respect to the "global", single-threshold results, are calculated as $(E_I^{SU} - E_I^{global})/E_I^{global}$, in the SU case, and correspond to 8.1% in training and 4.8% in validation.

Eventually, we replaced riverbanks mapped by visual interpretation with a riverbank layer mapped automatically and calculated E_I in the training area using the new layer; results are listed in Table I as well. The percentage gain using SUs (7.7%) is comparable to the results obtained with visual mapping of riverbanks (8.1%).

Table I. Numerical results from the comparison of eLIMs obtained with global thresholding and with grid-based and SU-based multi-threshold presented in this work and Ref. [5].

Riverbanks mapping		**Training**				**Validation**		
Visual	E_I	0.369	0.344	0.339		0.512	0.510	0.487
	Gain	-	6.7%	8.1%		-	0.4%	4.8%
Automatic	E_I	0.401	-	0.370		-	-	-
	Gain	-	-	7.7%		-	-	-

III. DISCUSSION AND CONCLUSIONS

The topography-driven, multi-threshold approach to landslide mapping from satellite imagery proposed in Ref. [5], and updated in this work, presents several advantages.

The numerical results of the comparison of the automatic mapping procedure with the ground-truth of an eLIM prepared by visual interpretation (Table I) reveal that the topographic-aware subdivision of the territory allows for a better classification performance both than thresholding applied globally, or within a topographic-blind subdivision. This is particularly true in the validation area, where the grid-based method shows little gain (0.4%) with respect to the global thresholding method.

PeerJ Preprints | https://doi.org/10.7287/peerj.preprints.27067v1 | CC BY 4.0 Open Access | rec: 30 Jul 2018, publ: 30 Jul 2018

In second place, we substantially simplified image preparation with respect to existing land cover classification methods using remote sensing. Considering the only "landslide" class reduces the time and effort needed to train the algorithm to distinguish the spectral response of landslides.

In third place, once the preliminary steps of SU delineation, g_{ls} training and calibration of thresholds are performed, the procedure is fully automatic, including the detection of riverbanks, left out of our previous work [5]. Class assignment is automatic and it does not require a-posteriori identification of the different classes. Figure 1 contains a table describing the different levels of automation of the various actions required to achieve multi-threshold classification.

In preparing the g_{ls} function map, we combined three indices embodying both radiometric (ΔNDVI and SA) and geometric (PCA) information contained in satellite images, to account for the heterogeneity showed by the spectral response of landslides [19,24]. Further developments may include different indices, in the discriminant function preparation, or additional topographic drivers [25]. The method can be used on a routinely basis, and run whenever the occurrence of a new landslide event is otherwise detected with specialized methods [6,23].

In conclusion, we argue that the improved performance and limited training requirements of the classification procedure represent a step forward towards an automatic, reliable real-time landslide mapping from satellite imagery.

REFERENCES

[1] Guzzetti, F., A.C. Mondini, M. Cardinali, F. Fiorucci, M. Santangelo, K. T. Chang, 2012. "Landslide inventory maps: New tools for an old problem". Earth-Science Reviews 112(12), 42-66.

[2] Marchesini, I., F. Ardizzone, M. Alvioli, M. Rossi, F. Guzzetti, 2014. "Non-susceptible landslide areas in Italy and in the Mediterranean region". Natural Hazards and Earth System Sciences 14, 2215-2231.

[3] Fiorucci, F., M. Cardinali, R. Carlà, M. Rossi, A. Mondini, L. Santurri, F. Ardizzone, F. Guzzetti, (2011). "Seasonal landslide mapping and estimation of landslide mobilization rates using aerial and satellite images". Geomorphology 129(12), 59-70.

[4] Casagli, N., W. Frodella, S. Morelli, V. Tofani, A. Ciampalini, E. Intrieri, F. Raspini, G. Rossi, L. Tanteri, P. Lu, 2017. "Spaceborne, UAV and ground-based remote sensing techniques for landslide mapping, monitoring and early warning". Geoenvironmental Disasters. 4(1):9.

[5] Alvioli, M., A. C. Mondini, F. Fiorucci, M. Cardinali, I. Marchesini, 2018. "Topography-driven satellite imagery analysis for landslide mapping". Geomatics, Natural Hazards & Risk 9(1), 544-567.

[6] Mondini, A.C., 2017. "Measures of spatial autocorrelation changes in multitemporal SAR images for event landslides detection". Remote Sensing 9(6).

[7] Borghuis, A.M., K. Chang, H. Y. Lee, 2007. "Comparison between automated and manual mapping of typhoon triggered landslides from spot 5 imagery". International Journal of Remote Sensing 28(8), 1843-1856.

[8] Martha, T.R., N. Kerle, C. J. van Westen, V. Jetten, K. V. Kumar, 2011. "Segment optimization and data-driven thresholding for knowledge-based landslide detection by object-based image analysis". IEEE Transactions on Geoscience and Remote Sensing. 49(12), 4928-4943.

[9] Rosin, P.L., J. Hervás, 2005. "Remote sensing image thresholding methods for determining landslide activity". International Journal of Remote Sensing. 26(6), 1075-1092.

[10] Mondini, A.C., K. T. Chang, 2014. "Combining spectral and geoenvironmental information for probabilistic event landslide mapping". Geomorphology 213, 183-189.

[11] Cheng, K., C. Wei, S. Chang, 2004. "Locating landslides using multi-temporal satellite images". Advances in Space Research 33(3), 296-301.

[12] Carrara, A., 1993. "Uncertainty in evaluating landslide hazard and risk". In: Nemec J, Nigg JM, Siccardi F, editors. Prediction and Perception of Natural Hazards: Proceedings Symposium, 22-26 October 1990, Perugia, Italy; Dordrecht. Springer Netherlands. p. 101-109.

[13] Guzzetti, F., A. Carrara, M. Cardinali, P. Reichenbach, 1999. "Landslide hazard evaluation: a review of current techniques and their application in a multi-scale study, Central Italy". Geomorphology 31, 181-216.

[14] Alvioli, M., I. Marchesini, P. Reichenbach, M. Rossi, F. Ardizzone, F. Fiorucci, F. Guzzetti, 2016. "Automatic delineation of geomorphological slope units with r.slopeunits v1.0 and their optimization for landslide susceptibility modeling". Geoscientific Model Development 9, 3975-3991.

[15] Schlögel, R., I. Marchesini, M. Alvioli, M. Rossi, P. Reichenbach, J.-P., Malet, 2018. "Optimizing landslide susceptibility zonation: effects of DEM spatial resolution and slope unit delineation on logistic regression models". Geomorphology 301, 10-20.

[16] Tucker, C.J., 1979. "Red and photographic infrared linear combinations for monitoring vegetation". Remote Sensing of Environment 8(2), 127-150.

[17] Sohn, Y., N. Rebello, 2002. "Supervised and unsupervised spectral angle classifiers". Photogrammetric Engineering and Remote Sensing 68(12), 1271-1280.

[18] Richards, J., X. Jia, 2006. "Remote sensing digital image analysis". Springer-Verlag Berlin Heidelberg, pp. 439

[19] Mondini, A.C., K. Tsung Chang, H. Yuan Yin, 2011. "Combining multiple change detection indices for mapping landslides triggered by typhoons". Geomorphology.134(34), 440-451.

[20] Delon, J., A. Desolneux, J. L. Lisani, A. B. Petro, 2007. "A nonparametric approach for histogram segmentation". IEEE Transactions on Image Processing 16(1), 253-261.

[21] Brakenridge, G., J. Syvitski, E. Niebuhr, I. Overeem, S. Higgins, A. Kettner, L. Prades, 2017. "Design with nature: causation and avoidance of catastrophic flooding, Myanmar". Earth-Science Reviews 165(Supplement C), 81-109.

[22] Fiorucci, F., D. Giordan, M. Santangelo, F. Dutto, M. Rossi, F. Guzzetti, 2018. "Criteria for the optimal selection of remote sensing images to map event landslides". Natural Hazards and Earth System Sciences 18, 405-417

[23] Mondini A. C., K. T. Chang, S. H. Chiang, R. Schlögel, C. Notarnicola, H. Saito, 2017. "Automatic mapping of event landslides at basin scale in Taiwan using a Monte Carlo approach and synthetic land cover fingerprints". Int J Appl Earth Obs Geoinf 63(Supplement C), 112–121.

[24] Mondini, A.C., F. Guzzetti, P. Reichenbach, M. Rossi, M. Cardinali, F. Ardizzone, 2011. "Semiautomatic recognition and mapping of rainfall induced shallow landslides using optical satellite images". Remote Sensing of Environment 115(7), 1743-1757.

[25] Blaschke, T., B. Feizizadeh, D. Hölbling, 2014. "Object-Based Image Analysis and Digital Terrain Analysis for Locating Landslides in the Urmia Lake Basin, Iran". IEEE J-STARS 7(12), 4806-4817

PeerJ Preprints | https://doi.org/10.7287/peerj.preprints.27067v1 | CC BY 4.0 Open Access | rec: 30 Jul 2018, publ: 30 Jul 2018